Formation of a Nacelle Inlet Ground Vortex in Crosswind

Derek A. Nichols[1], Bojan Vukasinovic[2], and Ari Glezer[3]
Georgia Institute of Technology, Atlanta, GA 30332-0405

Bradley Rafferty[4]
The Boeing Company

Abstract

The formation of a ground vortex by the suction flow into an axisymmetric nacelle in the presence of a ground plane and crosswind normal to the nacelle's axis is investigated in low-speed wind tunnel experiments. It is shown that the vortex formation near the ground plane is effected by near-surface shear that is induced between the crosswind flow and reversed flow due to the inlet suction. Comprehensive state maps of the dependence of the vortex evolution on the nacelle suction flow and crosswind speeds and on the ground plane elevation lead to scaling of these three formation parameters. Depending on the speeds of the inlet and cross flows, the incipient ground vortices can either be advected by the cross flow or, when the thrust developed by the inlet flow is sufficiently high, these vortices become aligned with the inflow and are ingested into the nacelle leading to time-dependent intensification of flow distortion at the fan face.

Nomenclature

D	=	inlet throat diameter	r	=	radial distance from vortex center
D_{core}	=	vortex core diameter	R	=	inlet throat radius
D_v	=	vortex diameter	T	=	thrust
f	=	suction blower operating frequency	u	=	x-component velocity
h_z	=	ground plane distance from inlet base	U_o	=	crosswind speed
IDC	=	circumferential distortion index	V	=	average inlet velocity
IDC_{max}	=	max circumferential distortion index	w	=	distance from wall
$\dot{m}$	=	mass flow rate	z	=	distance from ground plane
$\dot{m}_c$	=	mass flow rate at choking	Γ	=	vortex circulation
$\dot{m}^*$	=	$\dot{m}/\dot{m}_c$	θ	=	azimuthal coordinate
p_a	=	atmospheric pressure	ρ	=	ambient air density
p_o	=	total pressure			

[1]   Graduate Research Assistant, AIAA Member.
[2]   Senior Research Engineer, AIAA Member.
[3]   Professor, AIAA Fellow.
[4]   Aerodynamics Engineer, Boeing Test & Evaluation, AIAA Member

American Institute of Aeronautics and Astronautics

I. Background

Commercial aircraft engine nacelles must be designed to comply with the Code of Federal Regulations (CFRs) throughout all stages of flight including ground taxi, takeoff, climb, cruise, descent, and landing. Although the majority of the flight time is spent in cruise, optimal cruise design must be adjusted to accommodate the other operational stages of flight. During operation close to the ground, the performance of the aircraft engines can be strongly impacted by the presence of the surface and especially by the presence of crosswind that can significantly alter the air intake at the inlet [1]. Since the aircraft speed is relatively low close to the ground, the crosswind speed can be significant relative to the speed of the aircraft and can lead to three distinct flow artifacts: the formation of a fuselage vortex, inlet flow separation, and, when coupled with ground effect, a ground vortex [2,3].

Inlet flow separation can occur as a result of crosswind or during climb at steep angles [4,5]. Earlier experimental investigations at Georgia Tech focused on characterizing this flow separation for a range of intake and crosswind speeds [6,7], and various types of passive and active control methodologies were used to mitigate and sometimes completely suppress the ensuing internal windward side separation [6–8].

In addition to inlet flow separation, the crosswind can also lead to the formation of a ground vortex if in close proximity to the ground plane which not only induces additional significant distortion within the inlet plane but can also lead to ingestion of foreign objects. It was estimated that roughly 50% of all engines taken off for repair were damaged due to foreign object ingestion during ground operations [2]. The fundamental aspects of the ground vortex formation were studied using potential flow theory which, paired with some experimental observations, was predominantly attributed to the intensification of ambient vorticity [2,9]. Computational investigations indicated that the phenomenon is dependent on a source of vorticity existing in the flow and shows that the vortex characteristics are highly influenced by the vorticity generated on the ground [3]. The measurements of Wang and Gursul [10] demonstrated the effect of an increase in the crosswind speed on the ground vortex formation and showed that the vortex can initially start as a pair of counter rotating vortices in the absence of crosswind and develops into a single vortex when the crosswind is present. Murphy et al. [11] studied the effect of a horizontally moving ground plane to better simulate realistic takeoff conditions and observed that at low velocity ratios between the crosswind and intake speeds, the ground vortex is significantly different compared to a stationary ground plane. This vortex is weaker, steadier, and more symmetric relative to the static ground. Murphy and MacManus [12] studied the effects of the ground plane height and reducing the yaw angle to 60° from normal on the vortex and showed that a stronger vortex is observed at lower ground plane clearances and larger intake yaw angles. There have also been some limited attempts to demonstrate suppression of the ground vortex which have shown promising results in simulations using external jets such as fan reverser jets [13,14], pulsed jets [13,14], and 'sprinkler' jets [15]. The simulations of Shmilovich and Yadlin [15] showed that ground vortex ingestion can be completely suppressed when using 'sprinkler' actuation.

The present experimental investigations explore the effect of introducing a vertically-adjustable ground plane in close proximity to an inlet in a crosswind to investigate the formation of a ground vortex. When a ground vortex appears, it is characterized using several metrics such as its stability, circulation, and measured inlet distortion. Particular emphasis of this work is placed on the dependence of the onset and evolution of the ground vortex on independent variations in its

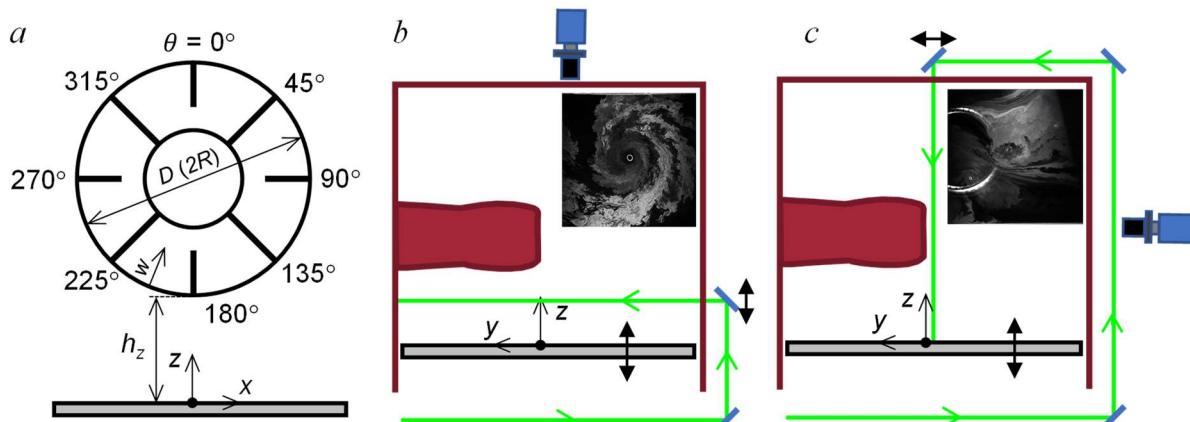American Institute of Aeronautics and Astronautics

primary formation parameters, namely the crosswind speed, nacelle mass flow rate, and the elevation of the nacelle above the ground plane.

II. Experimental Setup and Flow Diagnostics

The present experimental investigation is conducted in an open-return wind tunnel which was specifically designed to investigate the flow physics of nacelles in crosswind. The wind tunnel's test section has an adjustable ground plane and includes a model nacelle assembly mounted through its side wall, as shown Figure 1. The axisymmetric nacelle model (throat inlet diameter D) with conical centerbody of diameter $0.3D$ is mounted onto an axisymmetric duct that is driven in suction by a computer-controlled blower whose exhaust is driven into the ambient air through chilled water heat exchangers so that the ambient air temperature is maintained to within

Figure 1. *The crosswind wind tunnel test section showing the installed axisymmetric inlet and the moveable ground plane.*

1°C. The nacelle blower assembly is mounted on a moveable cart that enables its axial and lateral position within the test section to be adjusted. In the present investigation, the nacelle model is oriented normal to the cross flow and extends through half the width of the test section. The blower is driven at a prescribed mass flow rate $\dot{m}$ that is monitored using a pitot probe assembly within a calibrated straight pipe segment upstream of the blower's inlet (the nacelle duct chokes at some critical $\dot{m}_c$ which is used to define the present mass flow parameter $\dot{m}^* = \dot{m}/\dot{m}_c$). As noted above, the tunnel's test section is equipped with a vertically-adjustable ground plane (to within 0.01") that can be lowered up to $h_z = 1.6D$ below the bottom edge of the nacelle (Figure 2a). The cross flow in the test section is generated by an open-return, low-speed wind tunnel with a contraction ratio of 10:1 that is driven by a computer-controlled axial blower (flow uniformity in the empty test section within 1%). The present investigations emulate crosswind speeds up to $U_o = 35$ knots (18 m/sec).


Figure 2. *A rake of the total pressure probes relative to the ground plane (a) and the schematics of the PIV setup with moveable ground plane with horizontal (b) and vertical (c) flow illumination. Inset images illustrate the fields of view.*

American Institute of Aeronautics and Astronautics

Pressure recovery and flow distortion within the nacelle are assessed using a total pressure rake assembly that is located $0.45D$ downstream of the nacelle's lip at the characteristic position of the fan face. The assembly consists of 8 radial rakes that are equally distributed azimuthally (45°) with $\theta = 0°$ at the top of the inlet and increasing clockwise while alternating between 8 and 10 total pressure probes each, as shown in Figure 2a, with a higher density of probes at the wall. The rake total pressures are measured with a dedicated 96-channel pressure scanner with an uncertainty better than 1% of the time-averaged sample. For pressure measurements with higher temporal resolution, individual total pressure probes on the rake can be connected to high-frequency pressure transducers. The flow is also characterized using planar particle image velocimetry (PIV) as illustrated in Figures 2b-c where the laser sheet is oriented either parallel to the ground plane (Figure 2b) or to the inlet face (Figure 2c) to allow for tracking the motion of the ground vortex and calculating its circulation. Inset images illustrate instantaneous seeded flow for both configurations. The horizontal laser sheet illumination (Figure 2b) targets the vortex formation and ascent into the inlet, while the vertical laser sheet view (Figure 2c) enables the vortex tracking in the inlet.

In the present investigations, the vortex formation parameters including the nacelle's mass flow rate, crosswind speed, and ground plane elevation are each independently adjusted. The experiments are conducted either in time invariant conditions or during continuous (computer-controlled) time-monotonic variation of the mass flow rate while holding the other parameters constant. The time-monotonic cycle provides a data sweep for a given crosswind speed and ground plane distance, while the mass flow rate is ramped up/down at a fixed rate that is selected to be low enough to ensure a quasi-steady variation of the flow that closely reflects the corresponding steady-state measurements. The agreement between the time-monotonic and steady measurements was independently verified.
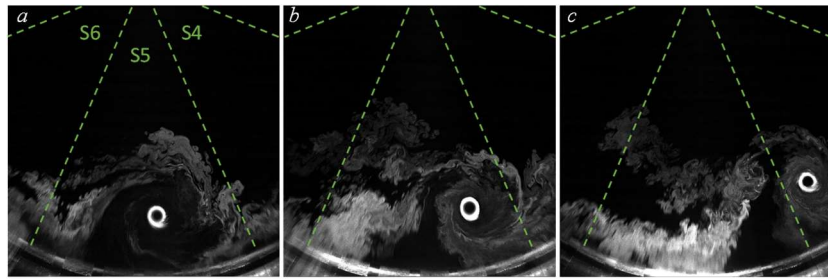
III. Ground Vortex Formation

The flow topology of an inlet in crosswind (e.g., [6,7]) becomes significantly more complex with the proximity to a ground plane during takeoff, landing, and ground roll and can lead to the formation of a ground vortex [2]. A realization of such a vortex in the present experiments is shown in Figure 3a. The flow in the test section is seeded with theatrical fog (the crosswind flow is from left to right) and the nacelle's inlet plane is illuminated with a spanwise-normal laser sheet as shown in Figure 2c. The clockwise (CW) vortex is visible above the nacelle's lower lip. Even
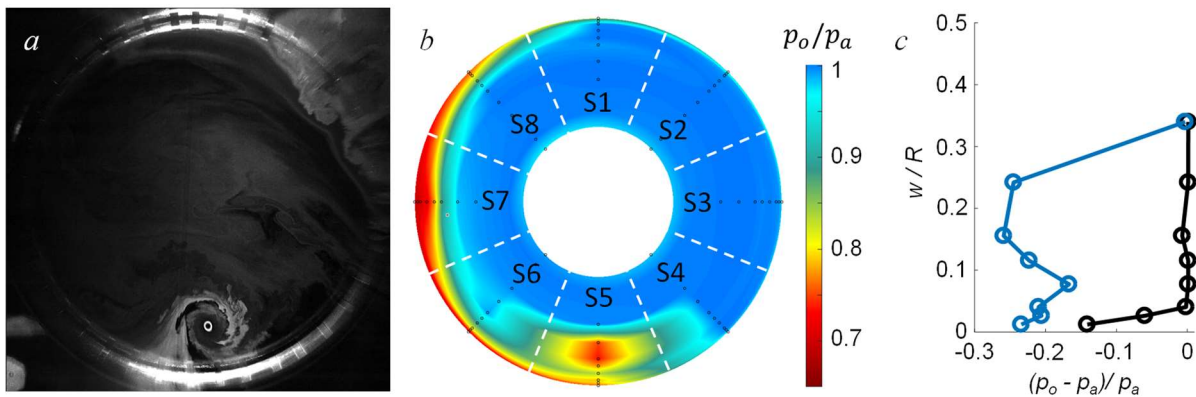
Figure 3. *A sample image of the seeded ground vortex (a), characteristic total pressure contour plot with the labeled vortex detection sectors S1 – S8 (b), and a sample of a total pressure profile for θ = 180° (c) in the absence (●) and presence (●) of a ground vortex.*

though the seeding particles do not reach the center of the core, it is marked by a ring of condensed water particles resulting from the core's low-pressure. The presence of the ground vortex is verified using a color raster plot of total pressure in Figure 3b that shows the characteristic pressure deficit within the core of the vortex and an additional low-pressure domain on the windward side of the nacelle's inner surface that is the result of local separation as discussed by Nichols et al. [6,7]. The radial distribution of the total pressures above the bottom surface of the nacelle at $\theta = 180°$ in the absence and presence of the vortex is shown in Figure 3c. In the absence of the vortex, the distribution shows the typical losses within the wall boundary layer ($w/R < 0.04$); however, in the presence of the vortex, the domain of the vortex's influence can be thought of as $0.11 < w/R < 0.24$ in which $(p_o - p_a)/p_a < -0.15$ where the minimum pressure occurs at $w = 0.16R$. These data also show the presence of a secondary low-pressure domain near the nacelle's surface ($w/R < 0.4$) that is indicative of the blockage brought about by the tangential motion induced by the vortex.

The radial pressure rakes are used to map the approximate position of the ground vortex within the nacelle for a range of the three primary parameters ($\dot{m}$, U_o, and h_z) by searching for the pressure minima within its core. The nacelle flow area is divided to eight sectors (S1 – S8) each

Figure 4. Sample images of the ground vortex ($\dot{m}^* = 0.75$ and $h_z = 0.36D$) for $U_o = 20$ (a), 25 (b), and 30 (c) knots. The dashed lines denote the boundaries of sectors S4, S5, and S6, for reference.

spanning 45° and centered about one of the rakes (Figure 3b). When a vortex is detected (by the off-surface minima of the total pressure), it is assigned to a given sector by considering the weighted pressure distributions of adjacent radial rakes. These pressure maps are updated at a rate of 2 Hz (high-speed videos showed that the characteristic azimuthal position of the vortex within this time window is within ±6°). An example is shown in Figures 4a-c in which $\dot{m}^*$ and h_z are invariant (0.75 and 0.36D, respectively) and U_o is varied. As U_o is increased from 20 (Figure 4a) to 25 (4b) to 30 (4c) kts, the vortex center moves counterclockwise from $\theta = 180°$ to 170° to 150°, respectively. This displacement of the core occurs between the rakes at 180° and 135° and the present detection algorithm assigns the vortices in Figures 4a and b to S5 (180°) and in Figure 4c to S4 (135°).

The presence of a ground vortex is investigated over a range of the formation parameters as described in §II and corresponding maps for varying inlet speed and ground plane height are shown in Figures 5a-c for crosswind speeds of 15, 25, and 35 kt, respectively. A given point on these maps indicates the presence of a ground vortex and identifies its sector (S4, S5, and S6) within the range of the mass flow rates and ground plane elevations. For a given elevation and crosswind speed, the nacelle mass flow rate is cycled at a constant rate (within 0.1 lb/sec) and if a vortex is detected using the procedure described in connection with Figure 3, it is marked in Figure 5 (the sectors are identified by color). The maps appear to be rather symmetric with respect to the cycling of the mass flow rate, indicating virtually no hysteresis. It is evident that as the crosswind speed increases, the presence of the vortex in the nacelle diminishes significantly with increasing ground plane elevation. However, it is also noted that as the crosswind speed increases, the vortex presence at low nacelle elevations becomes more pronounced. Finally, it is noteworthy that the ground plane
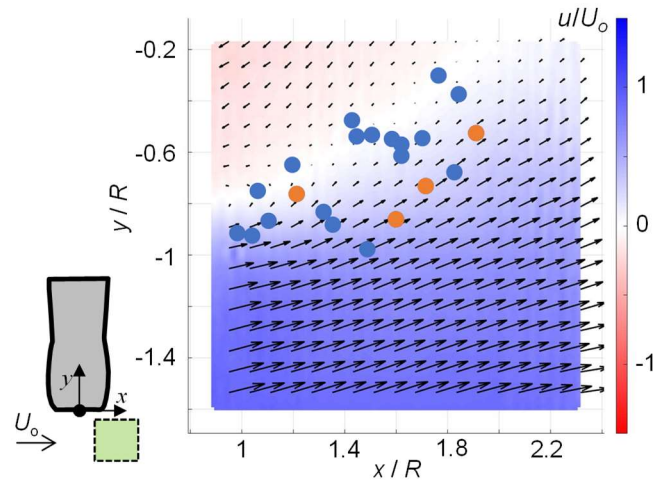
American Institute of Aeronautics and Astronautics
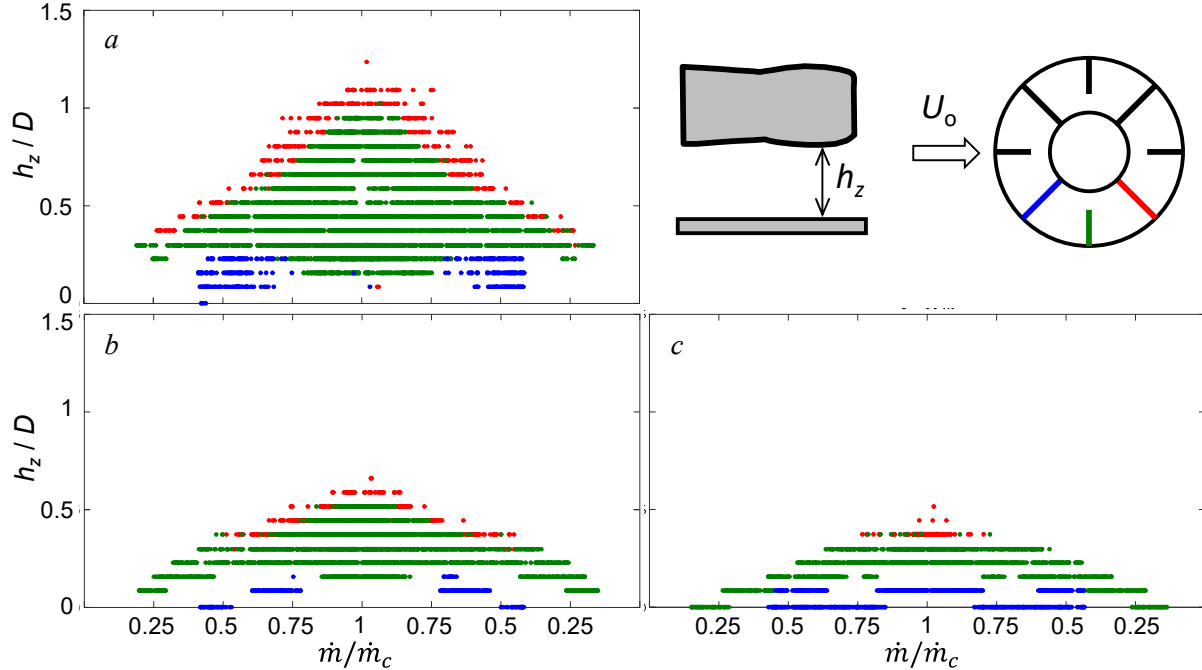
Figure 5. *State maps showing the ground vortex presence in sectors S4 (●), S5 (●), and S6 (●) for the varying ground plane height and inlet mass flow rates, and for crosswind speeds U_o = 15 (a), 25 (b), and 35 kt (c).*

distance and the inlet speed required for vortex formation are nearly linear for each crosswind speed albeit with slopes that precipitously decrease with cross stream speed.

At the low crosswind speed U_o = 15 kts (Figure 5a), the ground vortex first appears at h_z/D = 1.24 and θ = 135° for the highest flow rate values, though the vortex does not appear to be stable as it does not persist. At the next closest ground plane distance h_z/D = 1.1, the vortex first initiates as an unstable vortex at $\dot{m}^*$ = 0.85 and θ = 135° and becomes progressively more stable as the mass flow rate increases, as indicated by initial sporadic vortex detection, which becomes more consistent with increased intake speed. As the ground plane elevation decreases, the appearance of the vortex continues to occur earlier in the mass flow rate cycle. In addition, the vortex also becomes azimuthally displaced and is detected at S5 instead of S4 for $\dot{m}^*$ > 0.9 and h_z/D = 0.94. Overall, the vortex initiates around S4 and migrates clockwise towards the nacelle's windward edge with increasing inlet flow rate. This is opposite to the migration seen in Figure 4 which is associated with increasing crosswind speed. Hence, it may be concluded that the vortex moves towards the windward edge as the ratio between the inlet and crosswind speeds increases and in the opposite direction towards the leeward edge as this ratio decreases. As the ground plane elevation decreases, the vortex appears within S5 for $h_z/D \leq 0.3$ showing that the vortex moves towards the windward edge not only with increased nacelle flow rate but also with decreasing ground plane elevation. While the ground plane elevation and the nacelle flow rate at which the vortex appears vary nearly linearly, this variation is not linear when the vortex migrates from S4 to S5. Moreover, at the lowest ground plane elevation, the vortex appears even farther clockwise at S6. Similar to U_o = 15 kt, at U_o = 25 kt (Figure 5b) the vortex appears at S4 and moves towards the windward edge with increasing inlet speed or decreasing ground plane elevation, and the same trend continues for the map at U_o = 35 kt (Figure 5c). Overall, the data in Figure 5 indicate that, at least within this range of operating conditions, the vortex's most probable presence is within S5 and that once the vortex appears, it moves towards the windward edge with increased inlet speed.

If instead the crosswind speed were to increase while the other parameters remain fixed, the vortex will move towards the leeward side and could potentially dissipate. Finally, if the ground plane distance were to increase, the vortex would move towards the leeward side.

The boundaries of the map in Figure 5 that separate between the presence and absence of the ground vortex within the nacelle are further explored in an effort to search for a unified relation between the vortex formation parameters. Figure 6 shows a PIV color raster plot of the time-averaged streamwise velocity distribution superposed with velocity vectors within a horizontal plane measuring $0.7D \times 0.7D$ and $0.14D$ above the ground plane ($h_z = 0.36D$) such that its upstream edge is $0.45D$ downstream of the nacelle's centerline ($y = 0$ at the nacelle's inlet plane) as shown schematically in Figure 6. The flow conditions are selected to be on the boundary of the vortex map for which $\dot{m}^* = 0.65$, $U_o = 30$ kt, and $h_z = 0.36D$. The velocity distribution shows two distinct domains of forward and reversed

Figure 6. Ensemble-averaged PIV color raster plot of the streamwise velocity component superposed with velocity vectors, at elevation z = 0.14D off the ground plane ($\dot{m}^*$ = 0.65, U_o = 30 kt, h_z = 0.36D), where the measurement plane is shown in green in the schematics. Formed vortices are either advected downstream (●) or ingested into the inlet (●).

streamwise velocity that are separated by a crescent-shaped boundary on which the streamwise velocity nearly vanishes. The instantaneous PIV velocity data show the periodical presence of nominally vertical (ground) vortices within the shear region of the counter current domains. Simultaneous monitoring of the total pressure distributions within the nacelle showed that only a small number of these vortices (18% for the data of Figure 7) propagate upstream and are ingested into the inlet, and these measurements enable distinction between the vortices that become ingested into the inlet and those that are solely advected downstream. Even the vortices that are initially drawn into the inlet are unstable under these conditions and shortly afterwards can be overcome by the cross flow resulting in the vortex being pulled out of the inlet and shed downstream. In Figure 6, the instantaneous PIV images were used to identify and mark the appearance location of the vortices that are advected by the cross flow and those that are drawn into the inlet, and they are distinguished by color (blue and orange, respectively). As shown, the vortices form within the low velocity domain separating the forward and reversed streamwise velocity.

The critical conditions necessary for the ground vortex formation are determined by setting the crosswind speed and ground plane distance and incrementing the intake mass flow rate until the ground vortex first initiates. Resulting vortex formation cases are shown in Figure 7a. These data show the variation of inlet mass flow rate necessary to induce a ground vortex with the varying crosswind speed for a range of ground plane elevations and indicate that increasing the inlet flow rate or decreasing the crosswind speed enable the vortex to be advected upstream into the inlet. Conversely, decreasing the inlet flow rate or increasing the crosswind speed leads to streamwise advection with the cross flow. Consequently, for a given ground plane elevation, any combination of intake and crosswind speed above the corresponding line produces a ground vortex that is detected at the inlet while conditions below the line are insufficient for the vortex formation. When
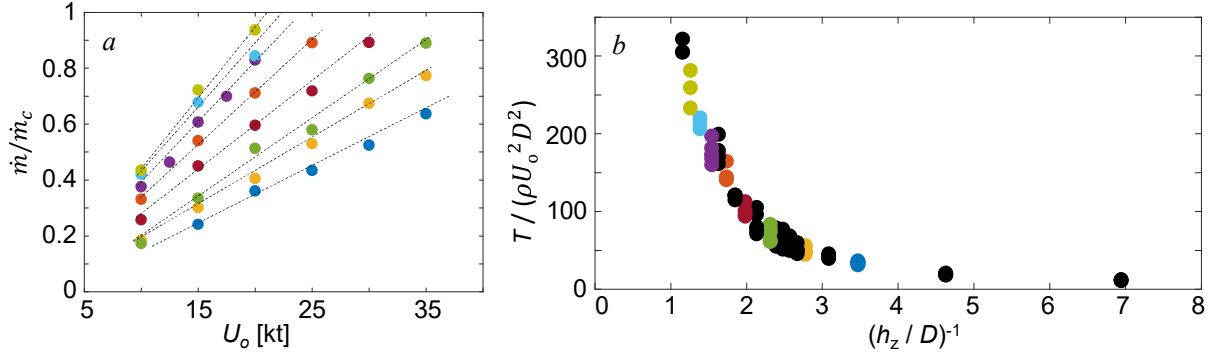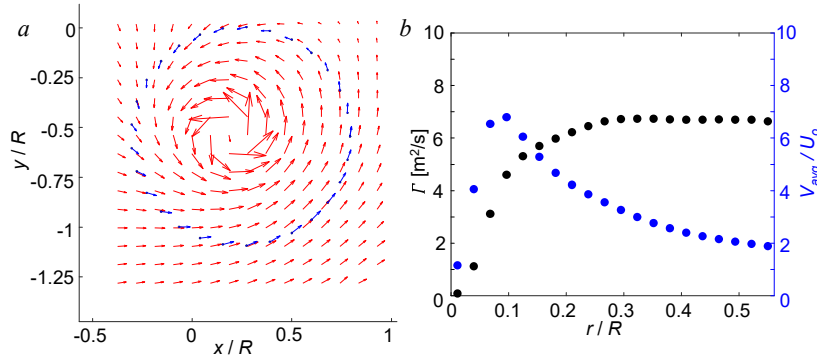
Figure 7. *Inlet mass flow rate for the ground vortex formation for the varying crosswind speeds (a) at different ground plane distances $h_z/D = 0.29$ (●), 0.36 (●), 0.43 (●), 0.50 (●), 0.57 (●), 0.64 (●), 0.71 (●), and 0.79 (●), and dimensionless inlet thrust as a function of the ground plane distance (b) with additional distances (●).*

these data are replotted in terms of the dimensionless thrust, $\dot{m}V/(\rho D^2 U_o^2)$ and the inverse of the ground plane distance $(h_z/D)^{-1}$, the data collapse onto a single curve $T/(\rho D^2 U_o^2) = f(h_z/D)$ as shown in Figure 7b indicating the importance of the thrust developed by the inlet flow to the formation of the ground vortex. The curve separates between realizable vortices (above) and no inlet vortices (below). As the ground plane elevation increases, the thrust must be sufficiently high to induce a ground vortex, asymptotically approaching an unattainable thrust level where vortex would cease to exist. On the other hand, as the ground plane elevation deceases, the critical inlet thrust for the vortex formation decreases, asymptotically approaching a small but nonzero thrust.

IV. Characterization of the Ground Vortex

Once the vortex is formed, its strength can be quantified by the circulation Γ about its axis. An illustration of the circulation estimate is shown in Figure 8. For a given flow condition, a sequence of PIV images is acquired in a plane that is parallel to the surface at some prescribed elevation z above the ground plane (as illustrated in Figure 2b). Since the ground vortex is not stationary, the following procedure is applied in order to extract its most probable realization. First, a vortex core identification scheme is applied in which the circular vortex core is identified through the local intensity peak detection, followed by a fitted circle and extraction of its center coordinates for each of the instantaneous realizations. A subset of the vortex population within $r = 0.06R$ about the averaged center is selected for further processing. The velocity field of each vortex within the subset is shifted until the vortex centers are clustered around the averaged center and an ensemble average is computed as shown in an example in Figure 8a. The vortex circulation $\Gamma(r)$ is


Figure 8. *Conditionally-averaged vortex velocity field ($\dot{m}^* = 0.75$, $U_o = 25$ kt, and $h_z = 0.36D$) at elevation $z = 0.29D$ above the ground plane (a), with interpolated vectors along a circle of radius $r = 0.58R$ about the vortex center (0.20R, -0.55R), and the corresponding radial variation (b) of the tangential velocity (●) and circulation (●).*
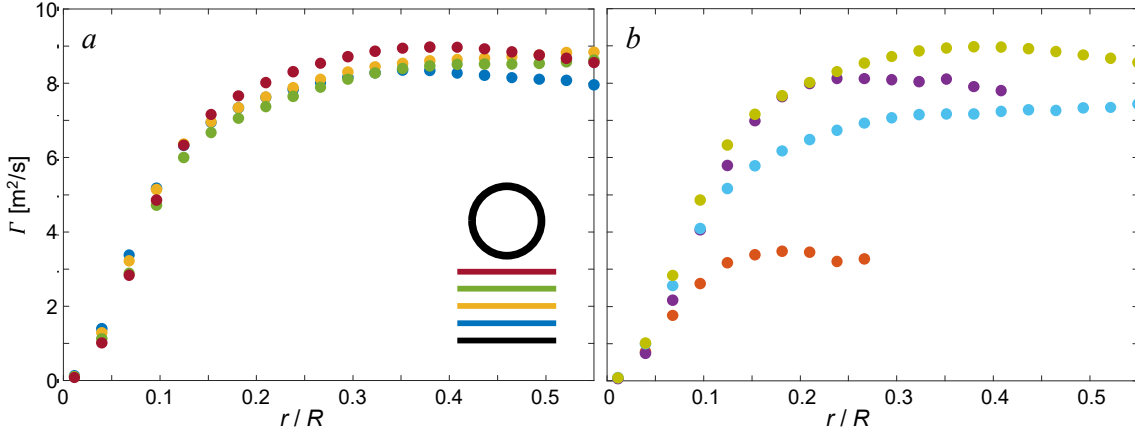
Figure 9. *Radial variation of the vortex circulation ($\dot{m}^* = 0.9$, $h_z = 0.36D$) for $U_o = 30$ kt at different elevations $z = 0.07D$ (●), $0.14D$ (●), $0.22D$ (●), and $0.29D$ (●) from the ground plane (a) and for the fixed elevation $z = 0.29D$, and varying crosswind speeds (b) $U_o = 15$ (●), 20 (●), 25 (●), and 30 kt (●).*

estimated using line integrals of the tangential velocity about circles of increasing radii r around the averaged center of the vortex as shown in Figure 8b (the radial variation of the tangential velocity is also shown for reference. The vortex circulation and its characteristic diameter are determined by the asymptotic level of the computed circulation (in the present example $D_v = 0.32D$ and $\Gamma = 6.75$ m²/s). The radial variation of the tangential velocity has a maximum $V_{max} = 6.9U_o$ at $r = 0.1R$ and is followed by an exponential decay to the cross flow speed.
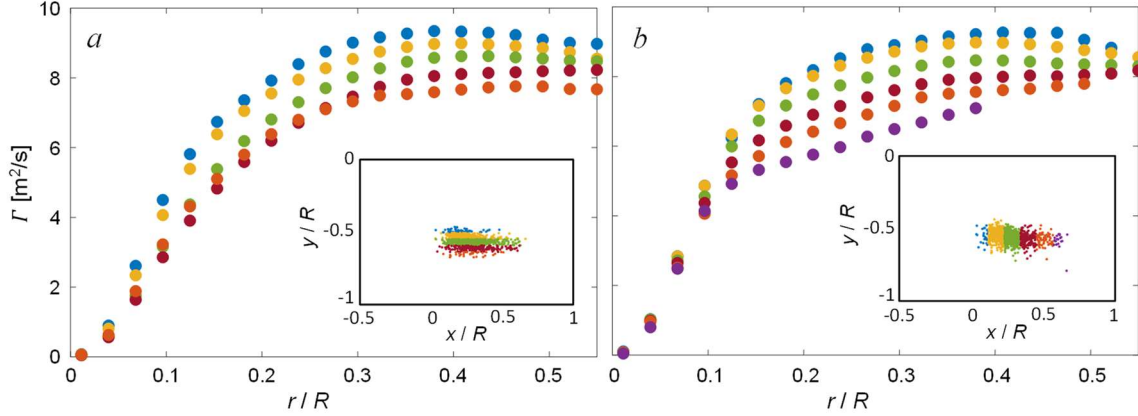
The variation of the vortex circulation with elevation above the ground plane, $\Gamma(r)$ is computed from similar velocity fields measured at $z = 0.07D$, $0.14D$, $0.22D$, and $0.29D$ above the ground plane surface at $h_z = 0.36D$ (Figure 9a). These data show that the circulation appears to be nearly invariant with r for all elevations through $r = 0.19R$ at which $\Gamma \approx 7.45$ m²/s, and for $r > 0.35R$ the circulation varies by less than 8% of the average asymptotic level 8.6 m²/s indicating that the core radius is nearly invariant with elevation until the vortex is in close proximity to the edge of the nacelle. Closer to the vortex center (up to $r/R < 0.1$) the circulation growth is somewhat steeper with increased proximity to the ground plane. It is also noted that the corresponding flow visualizations (not shown) indicate that the condensation ring in the vortex core increases in size with elevation, thus the low-pressure region is concentrated closer to the center of the vortex at lower elevations. Next, the effects of varying the crosswind speed is investigated at the fixed ground plane elevation $h_z = 0.36D$ in the plane $z = 0.29D$ above the ground plane at four crosswind speeds (Figure 9b). As expected, the diameter of the vortex, as estimated by the asymptotic levels of the circulation, increases with crosswind speed from about $0.18D$ at $U_o = 15$ kt to about $0.35D$ at $U_o = 30$ kt, but the vortex strength does not appear to increase monotonically with U_o exhibiting a drop at $U_o = 25$ kt. It is conjectured that this reduction in vortex circulation may be the result of an interaction between the vortex and flow separation on the windward edge of the nacelle [6] which may compete with the evolution of the vortex and results in reduced circulation and increased diameter (from $0.26D$ at $U_o = 20$ kts to $0.36D$ at $U_o = 25$ kts). Once the windward side flow separation is stabilized and the crosswind speed increases to $U_o = 30$ kts, the vortex is advected towards the leeward edge of the nacelle and its strength continues to increase with only a marginal increase in size (relative to $U_o = 25$ kt).

Even at a steady inlet flow rate and crosswind speed, the ingested ground vortex can meander within the surrounding inlet axial flow owing to unsteadiness associated with the counter current
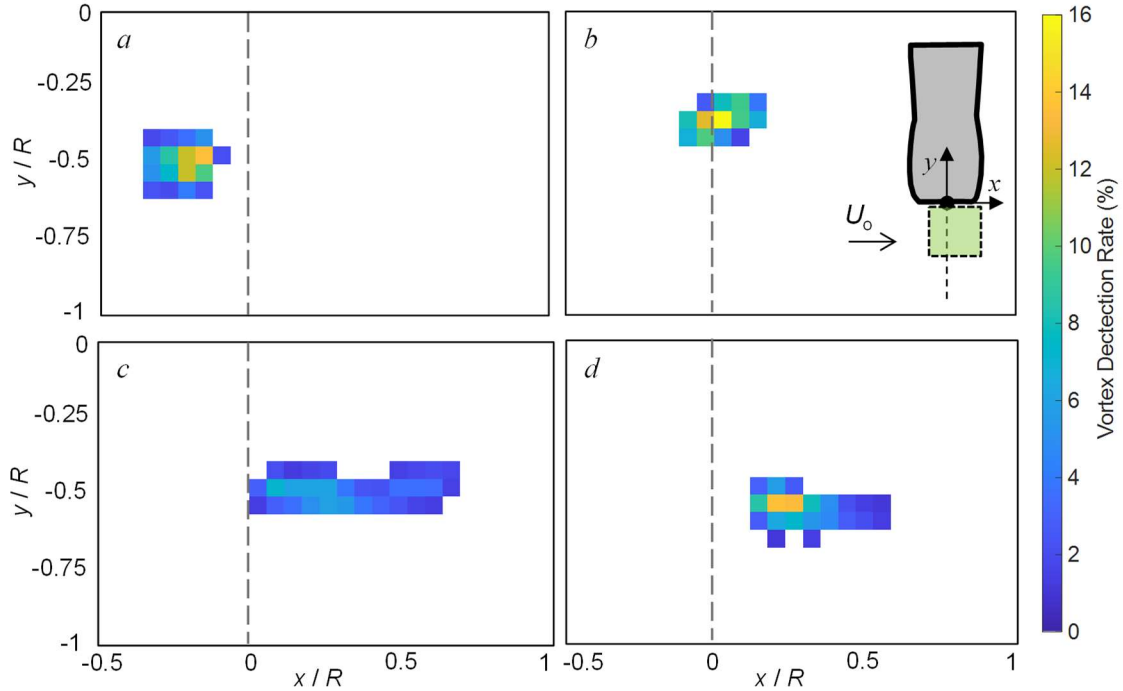
Figure 10. *Histograms of the positions of detected vortices in the plane z = 0.29D (ṁ* = 0.9, h_z = 0.36D) for the crosswind speeds U_o = 15 (a), 20 (b), 25 (c), and 30 kt (d). Projected inlet axis is shows as a dashed line for reference.*

flow that leads to its formation and disturbances that might be imposed by the interaction of the crosswind with the inlet flow. The unsteadiness of the subset of vortices that are ingested into the nacelle (Figure 9b), is assessed by considering their motion within a horizontal plane illuminated by a laser sheet at an elevation of $z = 0.29D$ above the ground plane ($0.07D$ beneath the inlet) as shown schematically in Figure 10. Similar to the processing of the data discussed in connection with Figure 8, the presence of these vortices is determined based on the appearance of the condensation pattern about the center of their cores and a histogram is formed based on their position within a square grid of bins each measuring $0.057R$ on the side. The histograms in Figure 10 are each formed using 1,000 images and the rate of detected vortices in each case at corresponding crosswind speeds of $U_o = 15$, 20, 25, and 30 kt is 79%, 86%, 88%, and 98%, respectively. Each histogram is normalized by the total number of detected vortices at the given crosswind speed so that each bin represents a relative frequency within that population. The projection of the nacelle's axis on this plane is also shown for reference ($x/R = 0$) while $y/R = 0$ coincides with the inlet plane of the nacelle. At $U_o = 15$ kt, the vortex population is rather compact and located on the windward side of the centerline and the largest fraction (14%) of the vortices appears at ($x = -0.14R$, $y = -0.48R$). As the crosswind speed increases to 20 kt (Figure 10b), the cluster becomes even more compact and migrates towards the centerline and is drawn closer to the nacelle's inlet plane (peak fraction 16% at $x = 0.03R$, $y = -0.37R$). This migration is in agreement with the analysis of Figure 5, and the compact cluster suggests that vortex stability increases with the crosswind speed. However, when the crosswind speed is increased to 25 knots (Figure 10c), the distribution of vortex locations changes significantly (peak fraction only 7% at $x = 0.09R$, $y = -0.48R$) and becomes skewed towards the leeward edge stretching from the centerline to $x = 0.75R$. As noted in connection with Figure 9b, this change in crosswind speed leads to a significant change in the evolution of the vortex circulation (it was conjectured that this change may be related to the

Figure 11. *The vortex circulation ($\dot{m}^* = 0.9$, $h_z = 0.36D$, $z = 0.29D$, and $U = 30$ kt) within the spanwise (a) and streamwise (b) domains binned over increments of 0.028D and 0.056D, respectively.*

onset of flow separation on the windward edge of the nacelle which may be unstable and contribute to the lateral meandering of the vortices). Finally, when the crosswind speed increases to 30 kt (Figure 10d), the cluster of vortex distributions becomes more compact (although still skewed laterally) and its center migrates farther downstream and somewhat farther away from the inlet plane (peak fraction 14% at $x = 0.20R$, $y = -0.54R$). The presence of a clear peak indicates that this cluster of vortices is more stable than in the previous realization.

Following the discussion in connection with the distribution of vortex populations in Figure 10, the dependence of the vortex strength on its spatial position on the ground plane relative to the inlet plane is investigated next using spanwise and streamwise histograms (Figures 11a and b, respectively) where the relative widths of the spanwise and cross stream bins are $0.028D$ and $0.056D$, respectively. The insets in Figures 11a and b show the populations within each group of bins. In this process, the bin-averaged circulation is computed by clustering the vortices in the instantaneous images at the center of each bin. Figure 11a shows that the circulation of the vortices within the spanwise bins decreases with distance from the inlet plane (by up to about 18% for the vortex displacement from y = -0.45R to about -0.65R relative to the inlet plane. Similarly, when considering the vortex's streamwise displacement away from the inlet centerline (Figure 11b), the vortices closest to the axis have the highest circulation which decreases with the streamwise displacement by up to 20% from x = 0 to about 0.6R. Clearly, both results point to increased vortex circulation with the increased proximity to the inlet. The only difference is how the circulation changes with displacement. Across the spanwise bins, the circulation increases monotonically with proximity to the inlet plane and with r/R, and ultimately asymptotes nearly simultaneously around $r/R \approx 0.38$ (Figure 11a). In the streamwise bins, the circulation is largely unchanged up to $r/R = 0.1$ (Figure 11b) but there is a significantly larger spread in the asymptotic levels. Nonetheless, these changes do not seem to significantly affect the vortex size, and all the bin-averaged vortices appear to have a similar diameter of about 0.4D within the measurement resolution. The present data also show that, for all the vortices in the population considered in Figure 11, the vortex core diameter defined as D_{core}, which is determined through the core identification scheme described above, is approximately normally distributed with a mean core diameter of 0.017D, such that the core is approximately 4% of the entire vortex diameter (Figure 12a). The distribution of the vortex core diameter with streamwise displacement of the vortex is shown in Figure 12b and does not point to any significant change, as it varies only by about 10% from the inlet axis to past 0.5R downstream,
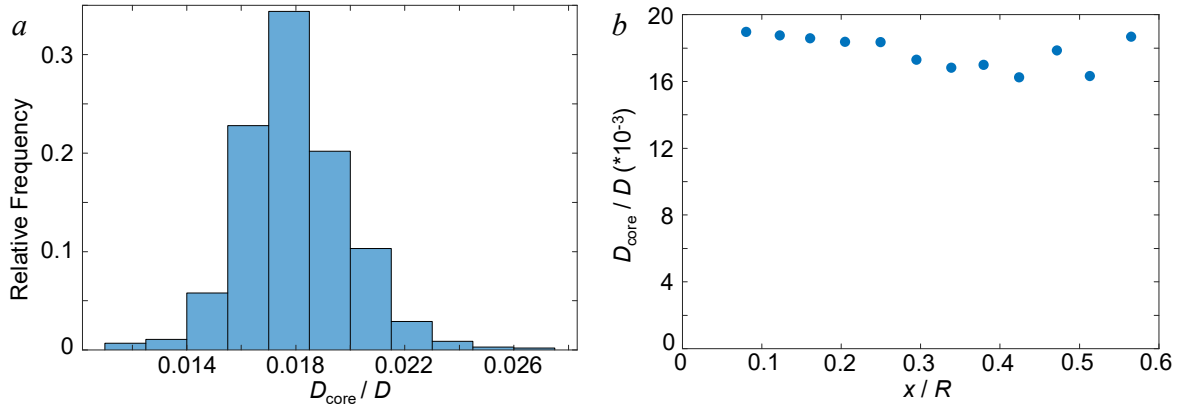
Figure 12. *Histogram (a) of vortex core diameter ($\dot{m}^* = 0.9$, $h_z = 0.36D$, $z = 0.29D$, and $U = 30$ kt) and its variation with axial distance from the inlet axis (b).*

with no obvious trend. This finding suggests that the vortex core size, although dependent on the test conditions, does not vary with the streamwise displacement of the vortex.

The motion of the vortex within the inlet is further investigated using time-resolved pressure measurements with pressure transducers sampled at a frequency of up to 500 Hz. Based on the vortex's movement within the inlet, each transducer is placed within Sectors S4 and S5 at a distance from the wall of $w = 0.12R$ and $0.24R$, respectively. Figure 13 shows an example of the vortex dynamics for $\dot{m}^* = 0.7$, $h_z = 0.36D$, and $U_o = 25$ kts. The pressure trace at S4 is exceptionally steady, exhibiting only a slight decrease relative to the ambient pressure indicating a small total pressure loss in the absence of the vortex. The measurements at S5, however, capture the vortex movement as is evident by the measured pressure fluctuations when the vortex moves closer or farther away from the sensor. Since the probe in S4 does not detect the vortex at all, it can be assumed that the vortex is predominantly within S5.

The pressure traces are also measured while the mass flow rate is cycled monotonically for $0.3 < \dot{m}^* < 0.75$ as described in connection with Figure 5, and the results are shown in Figure 14 for the same crosswind and ground plane elevation of Figure 13. At low intake speeds, both pressures are steady and virtually equal to the ambient pressure. However, as the inlet flow rate increases, the losses measured at S4 gradually increase as well. Eventually at $\dot{m}^* = 0.49$, the pressure measured at S4 begins to change intermittently as a result of the initial formation of the vortex on the leeward edge of the inlet, such that it is almost exclusively detected at the leeward transducer. As the inlet flow increases from $\dot{m}^* = 0.49$ to 0.56, the intermittent pressure drop continues to decrease as the vortex circulation increases and the pressure
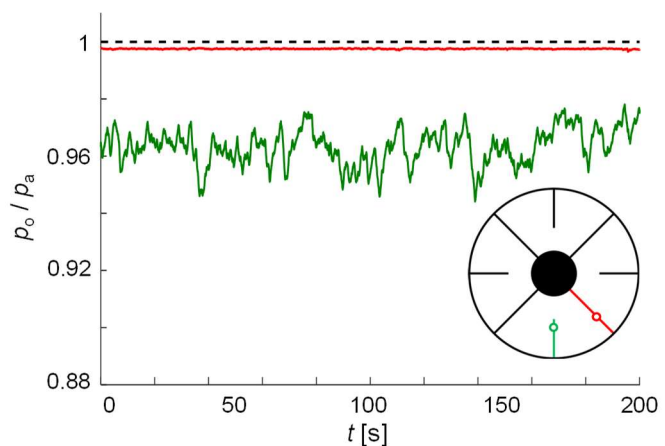
Figure 13. *Time-dependent total pressure for characteristic pressure ports in S4(●) and S5 (●) for $\dot{m}^* = 0.7$, $U = 25$ kt, and $h_z = 0.36D$. The ports are located at $w = 0.12R$ and $w = 0.24R$, respectively, away from the surface.*

American Institute of Aeronautics and Astronautics
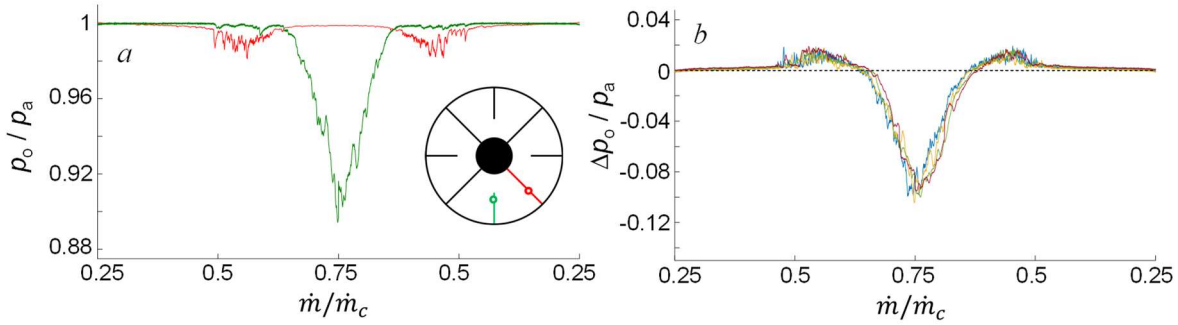
Figure 14. *Total pressure traces for pressure ports in S4 (●) and S5 (●) for U = 25 kt, h_z = 0.36D, as the inlet mass flow rate is ramped up and down from $\dot{m}^* = 0.3$ to 0.75 (a); and total pressure difference for the varying time rate of change of $\dot{m}^*$ (b) of 0.5f (●), f (●), 1.5f (●), and 2f (●).*

within the vortex core decreases. Although it might be expected that the vortex will continue to intensify with further increase in mass flow rate, the pressure reverses and begins to increase. This is attributed to the motion of the vortex away from S4 towards the windward edge and into S5. Aside from two small dips, the vortex is first detected at S5 when its signature vanishes at S4. Beyond $\dot{m}^* = 0.64$, the pressure at S5 proportionally decreases with the further increase in the mass flow rate, signaling an increase in vortex circulation and that the vortex likely keeps moving azimuthally clockwise towards S6. These measurements also point to the significant total pressure losses associated with the presence of the ground vortex that, depending on the inlet mass flow rate, can exceed 10% of the ambient pressure. To check how the sweep rate of the inlet flow affects the vortex dynamics, the time rate of change of the inlet flow rate $d\dot{m}/dt$ is adjusted between half and twice the nominal rate and the difference of the measured pressure traces is shown in Figure 14b for the different sweeping rates. These data show that, aside from occasional minor departures, all the pressure traces follow the same trend regardless of the sweep rate indicating that the vortex response is independent of the tested sweep rates.

V. Effect on Engine Fan Face

The total pressure losses and distortion over the engine's fan face in the presence of crosswind during takeoff and landing are of particular interest from the standpoint of overall engine performance. As is evident from Figure 3b-c, the presence of a ground vortex can further degrade the losses and distortions that are brought about by the crosswind and the proximity of the ground plane. Among the number of parameters that have been used to characterize the total pressure distortion of airplane engines [16], the parameter that was selected for the present investigations is the circumferential distortion index *IDC* [17]. The *IDC* characterizes the circumferential heterogeneity of the total pressure distributions over several fixed radii by computing the departures between the circumferentially-averaged and minimum total pressures over each. Finally, the maximum *IDC* index for given inlet conditions yields the maximum distortion parameter *IDC*$_{max}$ that is used to assess the total pressure distortion.

In the present experiments, *IDC* is measured in the absence and presence of the crosswind during a time-monotonic ramp up/down cycle of the inlet mass flow rate. Figure 15 shows traces of the variation of *IDC*$_{max}$ with the inlet's mass flow rate when the ground plane is fully removed and for $h_z = 0.36D$ (Figure 15a and b, respectively) for a range of crosswind speeds. As shown in Figure 15a (when the ground plane is retracted), in the absence of crosswind, the distortion starts at minimal levels and increases slightly with the inlet speed as a result of the viscous losses at the
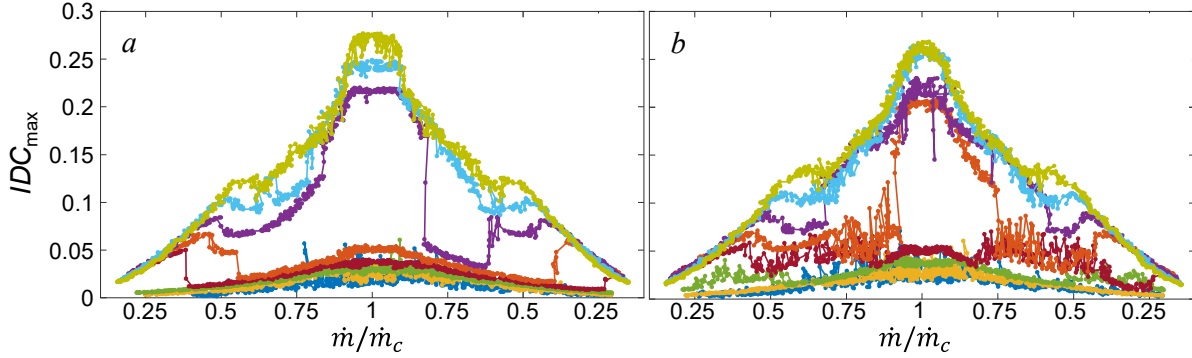
Figure 15. *Variation of the total pressure distortion parameter with monotonically-varying inlet mass flow rate cycle for U_o = 0 (●), 5 (●), 10 (●), 15 (●), 20 (●), 25 (●), 30 (●), and 35 (●) kt in the absence (a) and presence (b) of a ground plane at h_z = 0.36D.*

inner surface of the nacelle and ultimately diminishes as $\dot{m}/\dot{m}_c$ decreases. Aside from the increase in the absolute levels (that are relatively low), the trace shows occasional fluctuations (between 0.03 and 0.07) that are attributed to the sensitivity of IDC_{max} to fluctuations within the surface boundary layer. At low crosswind speeds (U_o = 5 and 10 kt) the distortion levels increase slightly compared to the base flow and also exhibit occasional fluctuations that increase in intensity with the inlet flow rate. As the crosswind speed increases from 10 to 15 kt, there is a significant increase in the rate of change of IDC_{max} with $\dot{m}^*$ for $\dot{m}^* < 0.38$. This increase is the result of separation on the windward inner surface of the nacelle [7]. With the further increase in intake speed ($\dot{m}^* > 0.35$), IDC_{max} drops precipitously to a level that is near that of the base flow as the separated flow reattaches with the increasing inlet mass flow rate [7]. This pattern reverses itself when the inlet flow decreases below $\dot{m}^* = 0.25$ albeit with some hysteresis. A similar trend is evident for U_o = 20 kt, but the reattachment is delayed to $\dot{m}^* > 0.55$ and experiences similar hysteresis as the previous case. The flow on the windward side remains separated when U_o = 25 knots although around $\dot{m}^* = 0.5$, the distortion level diminishes briefly and ultimately increases again. As shown by Nichols at al. [6,7], the separation initially spans a large azimuthal area on the windward side but as the inlet speed increases, the separation is pulled closer to the surface leading to a reduction in its radial penetration but with an increase in losses. The combination of these two opposing effects at first decreases the distortion as the measurement is dominated by the size of the separation and eventually increases the distortion as the pressure losses begin to rise. The ramp-down segment of the cycle at U_o = 25 kt is rather different from the ramp-up. The separated flow reattaches during ramp down at $\dot{m}^* = 0.82$ and as the mass flow rate continues to decrease, it reseparates for $\dot{m}^* < 0.62$ exhibiting a clear hysteresis relative to the ramp-up. Finally, for U_o = 30 and 35 kt, the flow does not reattach at any point during the cycle and the levels of distortion continue to increase with crosswind speed. The small momentary drops in distortion past $\dot{m}^* = 0.5$ are still observed even at the highest crosswind speeds, but the increases in total pressure losses quickly overcome any small gains due to the reduction of the separation domain at these crosswind speeds. Also, at the highest crosswind speeds, the prominent and persistent flow separation over the windward side appears to suppress the hysteresis effects. Overall, the distortion levels can reach upwards of 28% for the highest crosswind speed of 35 knots.

As the ground plane is positioned at $h_z = 0.36D$ (Figure 15b), IDC_{max} in the absence of cross flow and at U_o = 5 knots are nearly identical. However, at U_o = 10 kt there are significant fluctuations that are not present on the corresponding trace in Figure 15a. Inspection of the corresponding
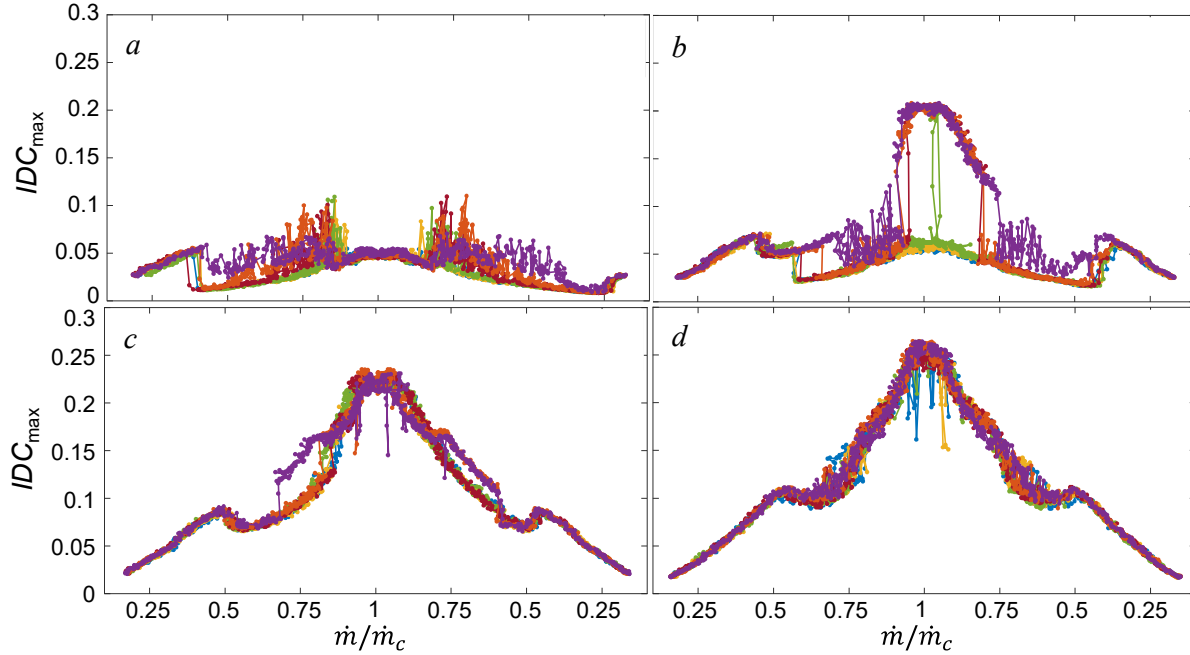
Figure 16. *Variation of the total pressure distortion parameter with monotonically-varying inlet mass flow rate cycle for U_o = 15 (a), 20 (b), 25 (c), and 30 (d) kt for ground plane elevations h_z = 0.72D (●), 0.65D (●), 0.58D (●), 0.50D (●), 0.43D (●), and 0.36D (●).*

pressure traces indicate that these fluctuations result from the passage of a ground vortex in the sector S5. It is noteworthy that when the vortex is present in S4, its effect on IDC_{max} is not as prominent since the total pressure losses are not yet as severe (cf., Figure 14a), thus a significant change in the distortion is not measured. For $\dot{m}^* > 0.55$, these perturbations diminish since the vortex moves farther towards the windward side such that its effect on the sector S5 is insignificant. As shown in Figure 5, for a fixed intake speed and ground plane elevation, the vortex moves towards the leeward edge as the crosswind speed increases. Therefore, higher inlet flow speeds are required to displace the vortex to S5 with increased crosswind speed. At $U_o = 15$ kt, the fluctuations in IDC_{max} are delayed to $0.4 < \dot{m}^* < 0.8$, and for $U_o = 20$ kt the fluctuations appear only at $0.7 < \dot{m}^* < 0.92$ before the flow ultimately separates as indicated by the sharp increase in IDC_{max} at $\dot{m}^* = 0.90$. Although the pressure traces show that the vortex still exists, the distortion is dominated by the separation. It is noteworthy that in the absence of the ground plane, the flow does not separate and, as shown in Figure 15a, it is attached for $\dot{m}^* > 0.55$. Consequently, it is argued that the proximity of the ground plane contributes strongly to distortion by promoting separation on the windward side of the nacelle, besides leading to the formation of the ground vortex. For $U_o \geq 25$ kt, the distortion curves do not exhibit the fluctuations that are prevalent at the lower speeds. The absence of these fluctuations may be explained by strong separation domains that dominate the pressure measurements, or by failure to detect vortices between adjacent sectors. Nevertheless, it is clear that the presence of the ground vortices leads to strong fluctuations that can lead to compressor blade vibrations and damage.

As noted in connection with the discussion of Figure 15, the proximity of the ground plane can trigger inlet flow separation, and this effect is further investigated using the flow distortion traces by incrementally increasing the ground plane elevation (by ~0.07D) from $h_z = 0.36D$ to $0.72D$ for a range of crosswind speeds (U_o = 15, 20, 25, and 30 kt in Figures 17a-d, respectively). For $U_o = 15$

American Institute of Aeronautics and Astronautics

kt, the traces of IDC_{max} follow the same general trend namely, starting with separation, attaching around $\dot{m}^* = 0.4$ and ultimately reaching an IDC_{max} level of 0.05 at the maximum flow rate. The difference between the traces is in the associated inlet flow rates for which the vortex occurs and the magnitude of the fluctuations that are associated with the presence of the ground vortex at S5. This is congruent with the discussion in connection with the ground vortex presence map in Figure 5 which showed that as the ground plane distance increases (while the other formation parameters are fixed), the ground vortex moves towards the leeward edge. For $U_o = 20$ kt (Figure 16b), the distortion traces are virtually identical for $\dot{m}^* < 0.55$; however, after this point, the flow becomes attached for the four most distant ground planes while the attachment is delayed (e.g., $\dot{m}^* = 0.65$ for $h_z = 0.43D$) with increased proximity of the ground plane. Eventually, for $\dot{m}^* > 0.9$, the flow reseparates for $h_z \leq 0.50D$. There is also a brief region of separation for $h_z = 0.58D$. These examples reflect the range of ground plane elevations in which the presence of the ground plane induces separation while there is no separation in its absence, thereby affecting the distortion. For $U_o = 25$ and 30 kt (Figures 17c and d), the inlet is separated the entire time regardless of the proximity of the ground plane although the ground plane can still have a slight impact on the distortion traces. For the two closest ground planes ($h_z = 0.36D$ and $0.43D$), the distortion exhibits an obvious increase for $0.65 < \dot{m}^* < 0.85$ which is the result of the ground vortex presence in S4 but otherwise, the distortion traces are nearly identical. When $U_o = 30$ kt (Figure 16d) the large fluctuations in the distortion at the highest inlet speeds for the farthest ground plane distances ($z = 0.65D$ and $0.72D$) result from periodic changes in the radial penetration of the separation which leads to rapid changes in distortion. It is noteworthy that these formation conditions occur near the border of the ground vortex map in Figure 5 and therefore it can be argued that the rapid changes in the distortion could result from the formation of the ground vortex within the inlet and its interactions with the separation.

These results show that the IDC_{max} generally increases with the inlet speed, except when the flow rate temporarily overcomes the crosswind-induced separation (as also discussed by Nichols et al. [7]). If the flow conditions are such that a ground vortex is formed, it can cause a significant temporal increase of over 150% in distortion. Additionally, the ground plane presence can at times trigger the flow separation which, in turn, can increase the distortion by over 300%.

VI. Conclusions

The present experimental investigations focus on the formation of a ground vortex by the inlet suction flow of an axisymmetric nacelle in the presence of a ground plane and crosswind normal to the nacelle's axis. It is shown that ground vortices originate along the crescent-shaped interface within the counter current shear layer that forms between the crosswind and the flow that is drawn into the nacelle. These ground vortices can be either advected in the streamwise direction without reaching the inlet, or past a critical inlet flow rate, a vortex can propagate upstream and can be ingested into the inlet. A vortex that is already ingested into the inlet can also be blown out due to momentary increase in the crosswind speed or a decrease in the inlet flow rate. Total pressure measurements at the fan face of the inlet show that if the elevation of the ground plane relative to the nacelle diminishes, the ingested vortex first moves towards the nacelle's leeward side and eventually vanishes once the distance surpasses a critical level (as in takeoff conditions).

Formation maps of the ground vortex that were assembled during the present investigations identify characteristic combinations of the three parameters (namely intake mass flow rate, crosswind speed, and ground plane distance) that enable the formation of a vortex off the ground plane and its ingestion into the inlet. The formation maps show that the critical inlet mass flow rate

needed for vortex formation and its detection within the nacelle varies nearly linearly with crosswind speed over a range of ground plane heights and that the rate of change increases with ground plane distance. Moreover, it is shown that vortex formation depends on the thrust developed by the inlet flow T such that the formation criterion has the (dimensionless) form $T/(\rho D^2 U_o^2) = f(h_z/D)$.

The fully formed ground vortex strength is characterized by its circulation, and the vortex characteristic cross-sectional scale is measured by the diameter at which the circulation becomes radially-invariant. This diameter is smallest near the ground plane, which is the primary source of the axial vorticity, and increases somewhat along the vortex centerline. It is shown that increasing the crosswind speed at a given inlet flow rate increases the vortex characteristic cross section but not necessarily its strength because an increase in the crosswind speed can induce separation along the inner surface of the nacelle's windward edge which can interfere and weaken the vortex strength. The present investigations show that when the vortex is ingested into the inlet, it can meander laterally by as much as $0.75R$ ostensibly as a result of the instabilities of the counter current shear layer that leads to its formation.

Finally, the presence of a ground vortex can further exacerbate the losses and distortions at the engine's fan face that are brought about by flow separation on the inner windward surface of the inlet lip owing to the presence of crosswind. The meandering of the vortex is typically characterized by time-varying oscillations of the pressure fluctuations that can contribute to noise and blade fatigue. Measurements of the distortion over a range of operating conditions in the absence and presence of the ground plane show that the presence of a ground vortex can result in a significant temporal increase of over 150% in distortion even in the absence of internal separation. Furthermore, if the vortex triggers separation, then the distortion can increase by over 300%.

Acknowledgment

References

[1] Trapp, L. G., Argentieri, H. G., de Souza, F. J., and Girardi, R. da M. "Aspects of Isolated Nacelles Near the Ground During Crosswind Operation." *ENCIT 2006*, 2006.

[2] Colehour, J. L., and Farquhar, B. W. "Inlet Vortex." *Journal of Aircraft*, Vol. 8, No. 1, 1971, pp. 39–43. https://doi.org/10.2514/3.44224.

[3] Trapp, L. G., and Girardi, R. "Evaluation of Engine Inlet Vortices Using CFD." *50th AIAA Aerospace Sciences Meeting including the New Horizons Forum and Aerospace Exposition*, No. January, 2012, *AIAA Paper 2012-1200*. https://doi.org/10.2514/6.2012-1200.

[4] Savelyev, A. A., Mikhaylov, S. V, and Zlenko, N. A. "Aerodynamic Inlet Design for Civil Aircraft Nacelle." *29th Congress of the International Council of the Aeronautical Sciences*, 2014, pp. 1–10.

[5] Maji, F., Efraimsson, G., and Reilly, C. J. O. "Potential Improvement of Aerodynamic Performance by Morphing the Nacelle Inlet." *Aerospace Science and Technology*, Vol. 54, 2016, pp. 122–131. https://doi.org/10.1016/j.ast.2016.04.006.

[6] Nichols, D. A., Vukasinovic, B., Glezer, A., DeFore, M. C., Rafferty, B., and Palacios, F. D. "Characterization and Control of Nacelle Inlet Flow in Crosswind." *AIAA Aviation*, 2019. *AIAA Paper 2019-3685*. https://doi.org/10.2514/6.2019-3685.

[7]   Nichols, D. A., Vukasinovic, B., Glezer, A., DeFore, M., and Rafferty, B. "Fluidic Control of Nacelle Inlet Flow in Crosswind." *AIAA Aviation*, 2020. *AIAA Paper 2020-2955*. https://doi.org/10.2514/6.2020-2955.

[8]   Nichols, D. A., Vukasinovic, B., Glezer, A., DeFore, M. C., and Rafferty, B. Steady and Unsteady Control of Nacelle Inlet Flow in Crosswind. *AIAA Scitech 2021 Forum*, *AIAA Paper 2021-1556*, 2021.

[9]   Siervi, F. D., Viguier, H. C., Greitzer, E. M., and Tan, C. S. "Mechanisms of Inlet-Vortex Formation." *Journal of Fluid Mechanics*, Vol. 124, 1982, pp. 173–207.

[10]   Wang, Z., and Gursul, I. "An Experimental Study of the Formation and Unsteady Characteristics of Inlet Vortices." *49th AIAA Aerospace Sciences Meeting Including the New Horizons Forum and Aerospace Exposition*, 2011. *AIAA Paper 2011-988*. https://doi.org/10.2514/6.2011-988.

[11]   Murphy, J. P., MacManus, D. G., and Sheaf, C. T. "Experimental Investigation of Intake Ground Vortices during Takeoff." *AIAA Journal*, Vol. 48, No. 3, 2010, pp. 688–701. https://doi.org/10.2514/1.45896.

[12]   Murphy, J. P., and MacManus, D. G. "Ground Vortex Aerodynamics under Crosswind Conditions." *Experiments in Fluids*, Vol. 50, No. 1, 2011, pp. 109–124. https://doi.org/10.1007/s00348-010-0902-4.

[13]   Johns, C. "The Aircraft Engine Inlet Vortex Problem." *AIAA's Aircraft Technology, Integration, and Operations (ATIO) 2002 Technical Forum*, October 2002, *AIAA Paper 2002-5894*. https://doi.org/10.2514/6.2002-5894.

[14]   Shmilovich, A., and Yadlin, Y. "Flow Control Techniques for Transport Aircraft." *AIAA Journal*, Vol. 49, No. 3, 2011, pp. 489–502. https://doi.org/10.2514/1.J050400.

[15]   Shmilovich, A., and Yadlin, Y. "Engine Ground Vortex Control." *AIAA Applied Aerodynamics Conference*, 2006, *AIAA Paper 2006-3006*. https://doi.org/10.2514/6.2006-3006.

[16]   Society of Automotive Engineers Aerospace Recommended Practice 1420 Revision B, 2002-03-01.

[17]   Colin, Y., Aupoix, B., Boussuge, J. F., and Chanez, P. "Numerical Simulation and Analysis of Crosswind Inlet Flows at Low Mach Numbers." *Proceedings of the 8th International Symposium on Experimental and Computational Aerothermodynamics of Internal Flows*, Nos. ISAIF8-0058, 2007.

American Institute of Aeronautics and Astronautics